

Femtosecond X-ray Fourier holography imaging of free-flying nanoparticles

Tais Gorkhover^{1,2,3*}, Anatoli Ulmer¹, Ken Ferguson^{2,3}, Max Bucher^{1,2,4}, Filipe R. N. C. Maia^{5,6}, Johan Bielecki^{5,7}, Tomas Ekeberg⁸, Max F. Hantke⁵, Benedikt J. Daurer⁵, Carl Nettelblad^{5,9}, Jakob Andreasson^{5,10,11}, Anton Barty⁸, Petr Bruza¹⁰, Sebastian Carron², Dirk Hasse⁵, Jacek Krzywinski², Daniel S. D. Larsson⁵, Andrew Morgan⁸, Kerstin Mühlig⁵, Maria Müller¹, Kenta Okamoto⁵, Alberto Pietrini⁵, Daniela Rupp¹, Mario Sauppe¹, Gijs van der Schot⁵, Marvin Seibert⁵, Jonas A. Sellberg^{5,12}, Martin Svenda⁵, Michelle Swiggers², Nicusor Timneanu^{5,13}, Daniel Westphal⁵, Garth Williams^{2,14}, Alessandro Zani⁵, Henry N. Chapman⁵, Gyula Faigel¹⁵, Thomas Möller¹, Janos Hajdu^{5,7,10} and Christoph Bostedt^{2,3,4,16}

Ultrafast X-ray imaging on individual fragile specimens such as aerosols¹, metastable particles², superfluid quantum systems³ and live biospecimens⁴ provides high-resolution information that is inaccessible with conventional imaging techniques. Coherent X-ray diffractive imaging, however, suffers from intrinsic loss of phase, and therefore structure recovery is often complicated and not always uniquely defined^{4,5}. Here, we introduce the method of in-flight holography, where we use nanoclusters as reference X-ray scatterers to encode relative phase information into diffraction patterns of a virus. The resulting hologram contains an unambiguous three-dimensional map of a virus and two nanoclusters with the highest lateral resolution so far achieved via single shot X-ray holography. Our approach unlocks the benefits of holography for ultrafast X-ray imaging of nanoscale, non-periodic systems and paves the way to direct observation of complex electron dynamics down to the attosecond timescale.

High-resolution imaging of single, non-periodic nanoparticles remains a great challenge. Electron microscopy requires the samples to be frozen and deposited on a substrate, potentially modifying their structure and functionality. Optical imaging techniques are limited in resolution. In contrast, intense femtosecond X-ray pulses from free-electron laser (FEL) sources enable 'diffraction-before-destruction'⁶ coherent diffractive imaging (CDI) of individual nanospecimens within a single exposure. Here, a single specimen is injected into the FEL focus from its native environment at room temperature and X-ray diffraction patterns are recorded long before the sample is vaporized by the FEL pulse^{5,7–9}.

The central problem of all indirect imaging methods, such as CDI, is the intrinsic loss of phase during the measurement. Thus,

structure recovery from CDI images is usually performed through iterative phasing algorithms that require solving a non-convex high-dimensional minimization problem. Much effort has been invested into the development of phase retrieval algorithms^{4,5,10–12}. Despite significant progress, structure reconstruction remains computationally demanding and requires guidance for selecting the object support. Noisy experimental data with missing data regions pose a particular challenge⁵ and sometimes lead to incompatible solutions⁴.

Holographic approaches overcome the phase problem by encoding the relative phase between the exit waves of a reference object and the sample^{13,14}. In lensless X-ray Fourier transform holography (FTH), a unique solution for the structure of the sample can be obtained from a simple two-dimensional Fourier transformation (2D FT)^{15–19}. The highly desirable combination of X-ray FTH and CDI of free nanoparticles has been discussed theoretically in the past^{15,17,19,20}. The experimental realization of lensless X-ray FTH^{15,21} with unsupported samples has not been achieved so far as it is very difficult to prepare a well-known and fixed reference with suitable spatial separation for randomly injected specimens.

Here, we demonstrate a proof-of-concept in-flight holography experiment, which in contrast to classical X-ray Fourier holography, does not require careful positioning or precise preparation of the reference. Instead, the reference scatterer is randomly placed, and its size and position are directly extracted from the diffraction image as schematically illustrated in Fig. 1. Diffraction from two equally sized spheres located in the plane perpendicular to the laser beam (Fig. 1a) is similar to Young's double slit experiment: the intensity distribution envelope in the reciprocal space reflects the size of the spheres and the fine intensity modulation mirrors the relative distance

¹Institut für Optik und Atomare Physik, Technische Universität Berlin, Berlin, Germany. ²Linac Coherent Light Source, SLAC National Accelerator Laboratory, Stanford, CA, USA. ³Stanford PULSE Institute, SLAC National Laboratory, Menlo Park, CA, USA. ⁴Chemical Sciences and Engineering Division, Argonne National Laboratory, Lemont, IL, USA. ⁵Laboratory of Molecular Biophysics, Department of Cell and Molecular Biology, Uppsala University, Uppsala, Sweden. ⁶NERSC, Lawrence Berkeley National Laboratory, Berkeley, CA, USA. ⁷European XFEL GmbH, Schenefeld, Germany. ⁸Center for Free-Electron Laser Science, DESY, Hamburg, Germany. ⁹Division of Scientific Computing, Department of Information Technology, Science for Life Laboratory, Uppsala University, Uppsala, Sweden. ¹⁰ELI Beamlines, Institute of Physics, Czech Academy of Science, Prague, Czech Republic. ¹¹Condensed Matter Physics, Department of Physics, Chalmers University of Technology, Gothenburg, Sweden. ¹²Biomedical and X-ray Physics, Department of Applied Physics, AlbaNova University Center, KTH Royal Institute of Technology, Stockholm, Sweden. ¹³Department of Physics and Astronomy, Uppsala University, Uppsala, Sweden. ¹⁴NSLS-II, Brookhaven National Laboratory, Upton, NY, USA. ¹⁵Wigner RCP, Institute for Solid State Physics and Optics, Budapest, Hungary. ¹⁶Department of Physics, Northwestern University, Evanston, IL, USA. *e-mail: taisgork@slac.stanford.edu

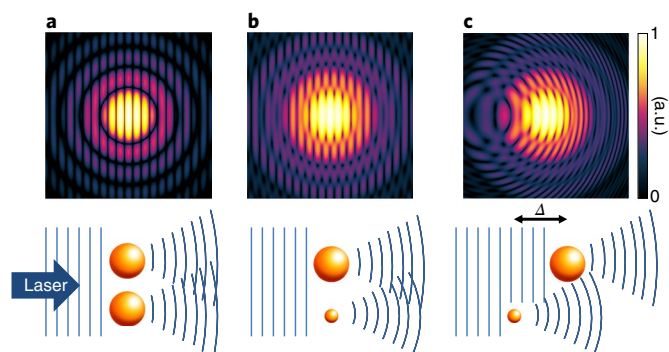


Fig. 1 | Principles of in-flight holography. Diffraction patterns in the first row are calculated from the objects and geometries displayed in the second row. **a**, The diffraction pattern produced by two equally sized spheres located in a plane perpendicular to the laser direction. It exhibits two dominant features. First, the ring-type envelope reflects the size of a single sphere. Second, fine straight modulation lines mirror the lateral distance between the spheres, similar to Young's double-slit experiment. **b**, If one sphere is considerably smaller than the other, a second envelope with wider ring spacing appears. Here, the different sizes of the spheres and the lateral distances are unambiguously encoded into the diffraction. **c**, The differently sized spheres are shifted along the laser direction. This shift Δ in real space translates into curvature of the fine modulation lines in the reciprocal space. The combination of distinct diffraction features such as the envelopes and fine modulations carry a unique 3D relative position map of the two spheres. This map is used for structure recovery in in-flight holography, where the large sphere is replaced by an unknown sample. The smaller sphere can be regarded as a source of a Fourier holography-type reference wave front.

between the spheres. Changes in the size of one sphere lead to an overlap of two characteristic envelopes (Fig. 1b). An offset along the laser direction results in a distinct curvature of the fine modulations (Fig. 1c). Vice versa, the patterns from the reciprocal space can be unambiguously translated into a real-space three-dimensional (3D) position map on the basis of the relative distances between the spheres that is directly encoded into the image. With in-flight holography, the smaller sphere can be regarded as a source of a reference wave front and the large sphere can be replaced by any unknown sample at a certain unknown distance. Using the information from the 3D map, the structure of the sample can be reconstructed via Fourier inversion of the diffraction pattern.

In our proof-of-principle experiment, we used almost spherical gas-phase Xe clusters with diameters of 30–120 nm as references and injected Mimi viruses with 450 nm quasi-icosahedral capsids as samples²². The experiment was carried out at the Linac Coherent Light source (LCLS) inside the LAMP end station²³, the experimental setup is illustrated in Fig. 2. We focused 100-fs-long X-ray FEL pulses with 1 nm wavelength to peak power densities up to 10^{17} W cm⁻², which are necessary for single-particle CDI.

The bio-sample and the cluster jets were overlapped inside the FEL focus using the instantaneous feedback from ion signal and X-ray diffraction patterns. The holograms were recorded using a p-n charge-coupled device (pnCCD) detector placed 735 mm downstream from the interaction region and covering up to a momentum transfer of $q = 0.3$ nm⁻¹.

A hologram of a Mimi virus is displayed in Fig. 3a. The real part of the Mimi virus image from a reconstruction based on a Fourier inversion of the hologram (discussed in detail in the next paragraph and in Methods) is displayed in Fig. 3b. The shape and the size of the Mimi virus are in perfect agreement with results from previous studies^{5,22} demonstrating that in-flight Fourier holography provides

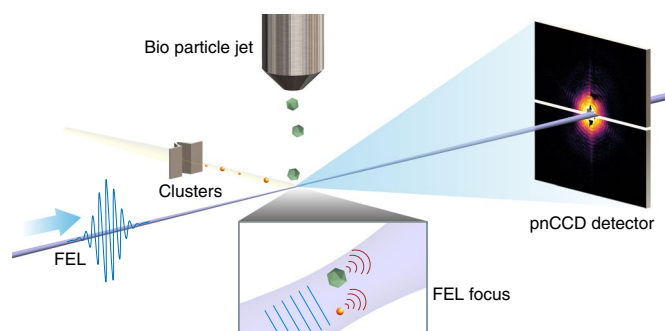


Fig. 2 | Experimental setup. The bioparticle jet and the Xe cluster jet are mounted perpendicular to each other and the FEL direction and overlapped inside the FEL focal volume. The X-ray photons diffract from randomly injected Xe clusters and nanosamples as schematically illustrated in the magnification panel. The resulting diffraction patterns are recorded on a pnCCD detector placed 735 mm downstream. The diffraction from the spherical clusters serves as a reference wavefront, similar to a pinhole-like source.

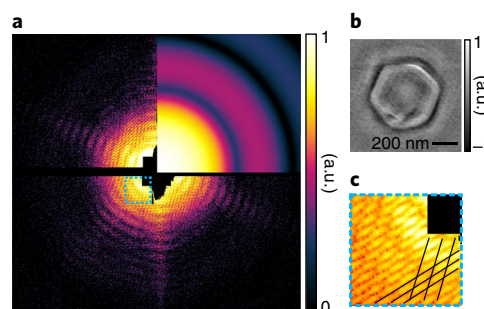


Fig. 3 | Hologram and reconstructions. **a**, Hologram of a Mimi virus. The signature envelope from the reference cluster is visualized in the upper right quadrant. **b**, The reconstruction of the Mimi virus from the hologram corresponds to a 2D projection of a quasi-icosahedron, as expected from previous experiments^{5,22,31}. Note that the reconstruction is based on a two-step Fourier inversion without any predefined assumptions **c**, Magnified section of the hologram shown in **a** with interference ripples marked by black lines. Two independent modulations indicate the presence of at least two reference scatterers.

a correct and unique real-space shape of the sample. The structural information was retrieved in only few steps without the need for complicated iterative procedures. Note that due to the missing data from the FEL passage hole in the detector, the reconstruction is low-frequency-filtered and dominated by edge contrast information akin to a dark-field microscopic image.

The reconstruction of the Mimi virus is guided by the information directly extracted from the hologram using the scheme described in Fig. 1. In reciprocal space, the diffraction pattern shown in Fig. 3a exhibits the characteristic streak pattern due to the quasi-icosahedral shape of the virus. The reference Xe cluster with the strongest signal produces the centrosymmetrical intensity distribution envelope fitted and highlighted in Fig. 3a, in the upper right quadrant of the hologram. From this envelope, we calculated the cluster diameter $d = 74$ nm using the Guinier approximation²⁴. The fine modulations (magnified in Fig. 3c) convey information about the relative distances between the Mimi virus and the reference clusters. Two independent modulations emphasized in Fig. 3c indicate the presence of at least two reference clusters.

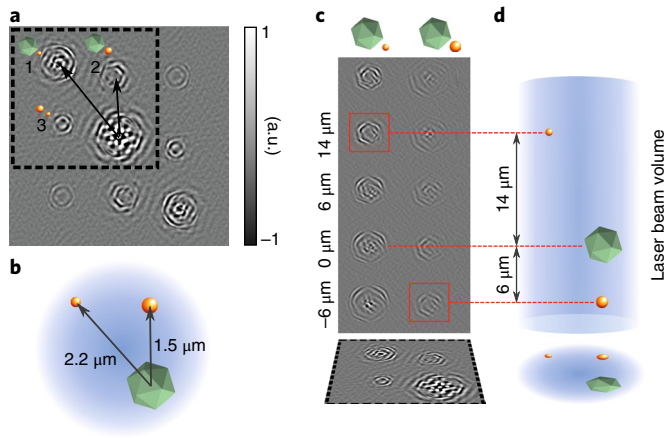


Fig. 4 | 3D reconstruction. **a**, 2D FFT of the hologram displayed in Fig. 3a. The cross-correlation terms (labelled 1–3) result from the interference between the spatially separated exit waves of the correlating particles and thus are displaced from the centre. Cross-correlation 1 can be attributed to a Mimi virus and a cluster with $d=74$ nm, cross-correlation 2 to a Mimi virus and a cluster with $d=100$ nm and cross-correlation 3 to clusters with $d=74$ and $d=100$ nm. The twin images of the cross-correlations are distributed point-symmetrically around the centre. **b**, The 2D FFT shown in **a** contains the positions of all three particles inside the plane perpendicular to the FEL. **c**, Using angular spectrum propagation, it is possible to recover the relative distances along the FEL axis. **d**, The combination of **a** and **b** creates a 3D map of two clusters and the Mimi virus. The fourth cross-correlation is not discussed here as the corresponding cluster is too far from the Mimi virus. Note that there is no need for several references to reconstruct the Mimi virus.

The features in the reciprocal space pattern shown in Fig. 3a,c can be directly translated into a real-space 3D map via two steps. First, a real-space 2D projection onto a plane perpendicular to the FEL is created from an inverse 2D FT of the hologram as presented in Fig. 4a. The highlighted region contains real-space cross-correlation terms (labelled 1–3) between objects contributing to the hologram. The cluster–cluster and Mimi–Mimi autocorrelation terms are concentrated around the centre of the FT. The distance between the centre of the FT and the cross-correlation terms is the relative distance between the cross-correlation partners in the plane perpendicular to the FEL propagation, as indicated by arrows in Fig. 4a,b.

The cross-correlations in Fig. 4a appear out-of-focus due to longitudinal offsets between the nanoparticles. Thus, in a second step, the cross-correlation terms are refocused using angular spectrum propagation^{14,18,19,25} as illustrated in Fig. 4c. The longitudinal distances between the objects can be recovered from a series of propagations into different planes perpendicular to the laser direction. Each propagation consists of a 2D FT of the hologram from Fig. 3a multiplied by a varying free-space propagator (see Methods). In a similar manner to refocusing with a microscope objective, the sharp boundaries of the cross-correlation terms emerge when the selected propagator term meets the real-space distance between the two correlating particles along the FEL axis as shown in Fig. 4c.

Both reconstruction steps combined create a 3D map of relative positions between the two clusters and the Mimi virus inside the FEL focal volume, as illustrated in Fig. 4d. For the final reconstruction of the Mimi virus presented in Fig. 3b, we used the refocused cross-correlation labelled 1 in Fig. 4a. The quality of the reconstruction was further enhanced through deconvolution with the reference cluster size determined from the envelope of the diffraction pattern as demonstrated in Fig. 3a (see Methods).

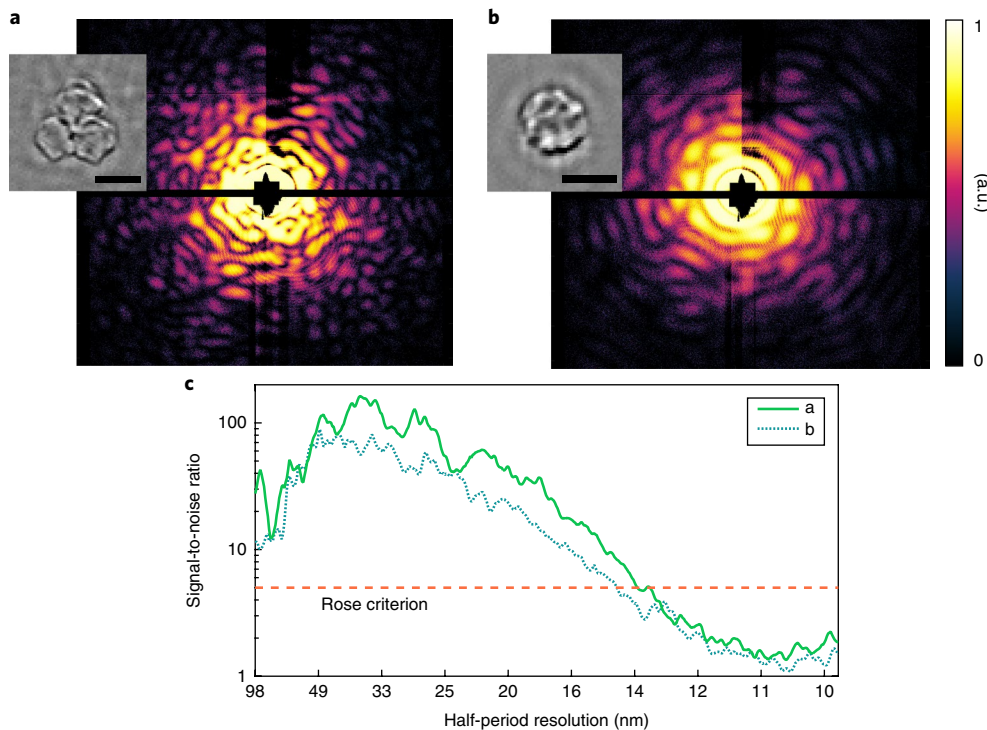


Fig. 5 | Holograms of deformed specimen recorded with small reference clusters. **a, b**, Holograms of specimens a and b and their reconstructions as insets. Scale bars, 200 nm. **c**, The corresponding signal-to-noise ratio versus the half-period resolution based on the Rose criterion. The central diffraction speckle from the reference cluster with a diameter of ≤ 20 nm covers almost the entire detector area.

We have shown that in-flight holography can provide high-fidelity images of highly asymmetrical samples. We recovered images from deformed specimens that have a more complex structure than the ideal Mimi virus. For example, the hologram in Fig. 5a was most probably recorded from a conglomerate of three samples, whereas the hologram shown in Fig. 5b stems from debris with a rich substructure. The reconstruction indicates that our method can be used to access the inner structure of a sample. The lateral resolution in our experiment was limited by the photon flux, as is the case in non-holographic studies^{5,6,26,27}. We achieved a lateral resolution below 20 nm as shown in Fig. 5c, and a 260 nm longitudinal resolution using small reference clusters with diameters of 30–40 nm (see Methods). In principle, the longitudinal resolution could be further improved by using softer X-rays².

In summary, our experiment is the first demonstration of high-fidelity imaging based on Fourier holography on free nanosamples. Our method is robust to noise, reliable and can be extended to a variety of references and samples. The contrast and resolution of the images obtained can be further improved at upcoming X-ray FEL facilities (see Methods for details). Given recent advances in single-shot imaging with table-top lasers²⁸, in-flight holography may reach laboratory-scale experiments due to its simplicity. This opens a novel avenue to study air pollution, combustion, cloud formation and catalytic processes on the nanoscale at the single-particle level. One could envision, for example, direct imaging of aerosol nucleation and droplet formation in their native environments without ensemble averaging effects¹. In-flight holography could also be easily extended to time-resolved studies of complex, ultrafast electron dynamics^{8,9,29,30}.

Methods

Methods, including statements of data availability and any associated accession codes and references, are available at <https://doi.org/10.1038/s41566-018-0110-y>.

Received: 26 July 2017; Accepted: 22 January 2018;

Published online: 26 February 2018

References

- Loh, N. D. et al. Fractal morphology, imaging and mass spectrometry of single aerosol particles in flight. *Nature* **486**, 513–517 (2012).
- Barke, I. et al. The 3D-architecture of individual free silver nanoparticles captured by X-ray scattering. *Nat. Commun.* **6**, 6187 (2015).
- Gomez, L. F. et al. Shapes and vorticities of superfluid helium nanodroplets. *Science* **345**, 906–909 (2014).
- van der Schot, G. et al. Imaging single cells in a beam of live cyanobacteria with an X-ray laser. *Nat. Commun.* **6**, 5704 (2015).
- Seibert, M. M. et al. Single mimivirus particles intercepted and imaged with an X-ray laser. *Nature* **470**, 78–81 (2011).
- Neutze, R., Wouts, R., van der Spoel, D., Weckert, E. & Hajdu, J. Potential for biomolecular imaging with femtosecond X-ray pulses. *Nature* **406**, 752–757 (2000).
- Chapman, H. N. et al. Femtosecond X-ray protein nanocrystallography. *Nature* **470**, 73–77 (2011).
- Bostedt, C. et al. Ultrafast X-ray scattering of Xenon nanoparticles: imaging transient states of matter. *Phys. Rev. Lett.* **108**, 093401 (2012).
- Gorkhovev, T. et al. Femtosecond and nanometre visualization of structural dynamics in superheated nanoparticles. *Nat. Photon.* **10**, 93–97 (2016).
- Miao, J., Sayre, D. & Chapman, H. Phase retrieval from the magnitude of the Fourier transforms of nonperiodic objects. *J. Opt. Soc. Am A* **15**, 1662–1669 (1998).
- Marchesini, S. et al. X-ray image reconstruction from a diffraction pattern alone. *Phys. Rev. B* **68**, 140101(R) (2003).
- Chapman, H. N. & Nugent, K. A. Coherent lensless X-ray imaging. *Nat. Photon.* **4**, 833–839 (2010).
- Gabor, D. et al. A new microscopic principle. *Nature* **161**, 777–778 (1948).
- Goodman, J. W. *Introduction to Fourier Optics* (Roberts and Company, Columbus, OH, USA, 2005).
- Eisebitt, S. et al. Lensless imaging of magnetic nanostructures by X-ray. *Nature* **432**, 885–888 (2004).
- Schlotter, W. et al. Multiple reference Fourier transform holography with soft x rays. *Appl. Phys. Lett.* **89**, 163112 (2006).
- Marchesini, S. et al. Massively parallel X-ray holography. *Nat. Photon.* **2**, 560–563 (2008).
- Geilhufe, J. et al. Extracting depth information of 3-dimensional structures from a single-view X-ray Fourier-transform hologram. *Opt. Express* **22**, 24959–24969 (2014).
- Guehrs, E. et al. Wavefield back-propagation in high-resolution X-ray holography with a movable field of view. *Opt. Express* **18**, 18922–18931 (2010).
- Shintake, T. Possibility of single biomolecule imaging with coherent amplification of weak scattering X-ray photons. *Phys. Rev. E* **78**, 041906 (2008).
- Chamard, V. et al. Three-dimensional X-ray Fourier transform holography: the Bragg case. *Phys. Rev. Lett.* **104**, 165501 (2010).
- Xiao, C. et al. Structural studies of the giant Mimivirus. *PLoS Biol.* **7**, 0958–0966 (2009).
- Ferguson, K. R. et al. The atomic, molecular and optical science instrument at the linac coherent light source. *J. Synchrotr. Radiat.* **22**, 492–497 (2015).
- Guinier, A. & Fournet, G. *Small-Angle Scattering of X-Rays* (Wiley, New York, USA, 1955).
- Bostedt, C. et al. Clusters in intense FLASH pulses: ultrafast ionization dynamics and electron emission studied with spectroscopic and scattering techniques. *J. Phys. B* **12**, 083004 (2010).
- Schropp, A. & Schroer, C. G. Dose requirements for resolving a given feature in an object by coherent X-ray diffraction imaging. *New. J. Phys.* **12**, 035016 (2010).
- Hantke, M. et al. High-throughput imaging of heterogeneous cell organelles with an X-ray laser. *Nat. Photon.* **8**, 943–949 (2014).
- Rupp, D. et al. Coherent diffractive imaging of single helium nanodroplets with a high harmonic generation source. *Nat. Commun.* **8**, 493 (2017).
- Zherebtsov, S. et al. Controlled near-field enhanced electron acceleration from dielectric nanospheres with intense few-cycle laser fields. *Nat. Phys.* **7**, 656–662 (2011).
- Gorkhovev, T. et al. Nanoplasma dynamics of single large xenon clusters irradiated with superintense X-ray pulses from the Linac coherent light source free-electron laser. *Phys. Rev. Lett.* **108**, 245005 (2012).
- Ekeberg, T. et al. Three-dimensional reconstruction of the giant Mimivirus particle with an X-ray free-electron laser. *Phys. Rev. Lett.* **114**, 098102 (2015).

Acknowledgements

We would like to thank J. Geilhufe, E. Guehrs, A. Schropp and S. Eisebitt for many helpful discussions. T.G. acknowledges the P. Ewald fellowship from the Volkswagen Foundation and the Panofsky fellowship from SLAC National Accelerator Laboratory. We would like to thank J. Segal and A. Tomada from SLAC for providing high-resistivity Si wafers. Parts of this research were carried out at the Linac Coherent Light Source (LCLS) at the SLAC National Accelerator Laboratory. LCLS is an Office of Science User Facility operated for the US Department of Energy Office of Science by Stanford University. This work is supported by the US Department of Energy, Office of Science, Office of Basic Energy Sciences, Division of Chemical Sciences, Geosciences, and Biosciences under contract no. DE-AC02-06CH11357 and contract no. DE-AC02-76SF00515. T.M. acknowledges financial support from BMBF (German Federal Ministry of Education and Research) projects 05K10KT2 and 05K13KT2 as well as DFG (German Research Foundation) BO3169/2-2. This work was supported by the Swedish Research Council, the Knut and Alice Wallenberg Foundation, the European Research Council, the Röntgen-Angström Cluster, ELI Extreme Light Infrastructure Phase 2 (CZ.02.1.01/0.0/0.0/15 008/0000162), ELIBIO (CZ.02.1.01/0.0/0.0/15 003/0000447) from the European Regional Development Fund, Material science and the Chalmers Area of Advance. F.R.N.C.M. acknowledges the Swedish Foundation for Strategic Research. Portions of this research were carried out at Brookhaven National Laboratory, operated under contract no. DE-SC0012704 from the US Department of Energy Office of Science. G.F. acknowledges the support of NKFIH K115504.

Author contributions

T.G. conceived the concept of 'in-flight' holography with two sources with support from C.B., T.M. and J.H. The project was led by T.G., C.B., F.R.N.C.M. and J.H. The experimental setup was designed and the experiment was performed by all authors. The bioparticle injector was operated by J.B., M.Sei. and K.M. The cluster source was operated by K.F., M.B., C.B. and T.G. The biological samples were prepared by D.H., D.S.D.L., K.O. and M.Sve. The online and offline data analysis was carried out by F.M., T.E., M.F.H., B.J.D., C.N., A.M., G.v.S., M.B. and K.F. The images were analysed and processed by A.U. and T.G. The results were interpreted by A.U. and T.G. with input from C.B., G.F., T.M., F.R.N.C.M. and J.H. The manuscript was written by T.G. and A.U. with contributions from C.B., G.F., T.M., F.M. and J.H. and input from all authors.

Competing interests

The authors declare no competing interests.

Additional information

Reprints and permissions information is available at www.nature.com/reprints.

Correspondence and requests for materials should be addressed to T.G.

Publisher's note: Springer Nature remains neutral with regard to jurisdictional claims in published maps and institutional affiliations.

Methods

Experimental methods. The experiments were performed at the LAMP instrument inside the AMO end station at the Linac Coherent Light Source (LCLS)³². We used soft X-ray pulses with 1200 eV photons and pulse energies up to 2 mJ at a 120 Hz repetition rate. The FEL beam is focused by a pair of Kirkpatrick–Baez mirrors to achieve the FEL intensities necessary for single-particle imaging. The biological samples were injected in a solution through a gas dynamic virtual nozzle using a guiding helium gas flow²⁷. The particle jet was focused down to a 100 μm diameter with an aerodynamic lens stack consisting of six apertures. The solvent evaporates during the injection. The Xe clusters were produced via a supersonic expansion through a conical nozzle with a diameter of 200 μm and an half opening angle of 4°, which was attached to a commercial Parker Series 99 pulsed valve. The mean cluster size was varied between 30 and 120 nm in diameter by adjusting the backing pressure of the gas reservoir (from 7 bar to 30 bar) and the nozzle temperature (from 240 to 300 K). It has been demonstrated in previous experiments that within the achieved resolution (down to 8 nm) the large majority of Xe clusters are spherical^{30,33}. We operated the source at a repetition rate of 10–30 Hz with regard to the gas load faced by the vacuum pumps under high Xe backing pressure. The timing of the pulsed cluster jet was synchronized to the FEL based on the overall hit rate. We optimized the cluster source timing to match the centre of the main cluster jet pulse with the arrival time of the FEL pulse. In this regime, the cluster size did not depend on the timing³⁴. The particle jet was skimmed down with a system of two fixed skimmers and an adjustable piezo skimmer, reaching a cluster jet width between 500 μm and 3 mm.

The X-ray diffraction patterns were recorded via a pnCCD detector pair with 75 $\mu\text{m} \times 75 \mu\text{m}$ pixel size and 1,024 \times 512 pixels per detector half. The two detector parts were positioned 735 mm downstream from the interaction region.

Requirements for coherence. The longitudinal coherence of LCLS pulses in the soft X-ray regime has been estimated to be 0.5 fs, which translates to 0.17 μm in real space³⁵. In principle, forward scattering from two objects placed with an offset along the FEL beam always leads to a coherent superposition of the scattered wave fronts. Constructive interference at scattering angles greater than zero can occur when the path length difference between the wave fronts is smaller than the longitudinal coherence. In our case, interference at the outer edge of the detector can be expected from reference–sample pairs with a maximum longitudinal distance of around 60 μm .

Structure reconstruction. Reconstruction of the structure from a X-ray hologram can be divided into three steps and is described below in greater detail. First, the images were calibrated and masked for detector imperfections. Second, the 3D composition between the sample and the reference was reconstructed. Third, the 3D information was used to refocus and refine the image of the sample through deconvolution.

Image imperfections. The intrinsic noise of the detector was subtracted using dark calibration and common mode correction (CM). CM correction is performed line-by-line and aims to remove the low-frequency noise in the readout electronics (details of the applied algorithm can be found in ref. ³⁶). The noise level of the recorded image was minimized by a correction for background X-ray scattering from the beam line and readout artifacts^{36,37}.

A binary mask from missing, dead, highly fluctuating and saturated detector pixels was generated for each diffraction pattern. The transition from masked areas to the real signal was smoothed out to suppress reconstruction ringing artifacts from an oscillating point spread function. This was accomplished by dilating the binary mask by 5 pixels and applying a Gaussian filter with $\sigma = 5$ pixels, to ensure a continuous transition to zero. We found that such localized mask–signal transition smoothing leads to negligible changes in the reconstruction of the specimen, while ringing in the surrounding areas is efficiently suppressed.

3D reconstruction. The samples and the reference clusters are almost transparent to the X-rays and thus the Born approximation is valid. In the far-field and small-scattering-angle region, the X-ray diffraction patterns O equal the absolute square of the Fourier transform of the projection of the object's electron density o along the FEL axis:

$$O(\mathbf{q}_\perp) = |\mathcal{F}[o(\mathbf{x}_\perp)]|^2 \quad (1)$$

Here \mathbf{x}_\perp and \mathbf{q}_\perp denote the coordinates perpendicular to the FEL beam in real space and the scattering vector in momentum space, respectively. By introducing a reference scatterer $r(\mathbf{x}_\perp - \mathbf{x}_\perp^0)$, the exit waves of both particles interfere and the X-ray diffraction patterns can be regarded as a Fourier hologram. In principle, the Fourier hologram contains 3D information that is limited by depth-of-field (DOF)¹⁸. DOF describes the maximum distance along the beam axis under which two features can be resolved simultaneously. It is important to note that our samples are smaller than the DOF and thus the exit wave of each specimen can be interpreted as a projection of its electron density. At the same time, the distance between the references and the samples along the FEL axis is mostly larger than the DOF. Therefore a 3D map with the positions of the individual nano-objects with regard to each other can be extracted from the hologram.

In the first step of the reconstruction, a single inverse Fourier transformation of the recorded 2D hologram $H(\mathbf{q}_\perp)$ can be regarded as a translation from momentum space coordinates to real space coordinates and results in the Patterson map $P(\mathbf{x}_\perp)$:

$$\begin{aligned} P(\mathbf{x}_\perp) &= \mathcal{F}^{-1}H(\mathbf{q}_\perp) \\ &= \mathcal{F}^{-1} \frac{4\pi^2}{\lambda^2 D^2} |\mathcal{F}(o(\mathbf{x}_\perp) + r(\mathbf{x}_\perp - \mathbf{x}_\perp^0))|^2 \\ &= \frac{2\pi}{\lambda^2 D^2} (o^*(-\mathbf{x}_\perp) \otimes o(\mathbf{x}_\perp) \\ &\quad + r^*(-\mathbf{x}_\perp + \mathbf{x}_\perp^0) \otimes r(\mathbf{x}_\perp - \mathbf{x}_\perp^0) \\ &\quad + o^*(-\mathbf{x}_\perp) \otimes r(\mathbf{x}_\perp - \mathbf{x}_\perp^0) \\ &\quad + r^*(-\mathbf{x}_\perp + \mathbf{x}_\perp^0) \otimes o(\mathbf{x}_\perp)). \end{aligned} \quad (2)$$

where λ is the X-ray photon wavelength and D is the detector distance. Here \otimes describes the convolution operator and the terms $o^* \otimes o$ and $r^* \otimes r$ are the autocorrelation functions without direct phase information. In the momentum space, the relative phase information is stored in the interference patterns between the reference and the sample wave fronts. The Patterson function translates this information into relative distances in the real space embodied by cross-correlation terms $o^* \otimes r$ and $r^* \otimes o$ as illustrated in Fig. 4a). Here, the 2D Patterson function of the Mimivirus hologram is shown. The autocorrelation terms are located in the centre of the Fig. 4a). The cross-correlation terms 1–3 between the reference clusters and the Mimivirus are located laterally shifted from the centre. The lateral shift of the cross-correlation terms arises from the lateral distances between the cross-correlation partners. With some knowledge about the reference (in our case: the size and spherical shape, which can be directly extracted from the hologram from a Guinier fit), these terms allow for unambiguous reconstruction of the sample's exit wave and thus the sample's structure. The lateral distance of the cross-correlation partners has to be at least twice the sample size in real space to avoid overlapping of the cross-correlation terms with the autocorrelation function in the Patterson map.

In the second step, the cross-correlation terms were refocused using the free-space propagator. The sample and the reference clusters were randomly injected into the FEL focal volume with an offset between the sample and the reference along the optical axis as demonstrated in Figs. 1 and 4. Consequently, the sample's exit wave propagates over a distance z before it interferes with the reference exit wave or vice versa. Assuming free propagation along the FEL beam (in the z direction) the sample's structure can be recovered by propagating the exit wave to the plane of the sample using the angular spectrum propagation $\psi_R(x, y, z)$ ¹⁴:

$$\psi_R(x, y, z) = \mathcal{F}^{-1} e^{iz} \sqrt{k^2 - q_x^2 - q_y^2} H(q_x, q_y) \quad (3)$$

with the wave field vector $\mathbf{k} = \frac{2\pi\mathbf{r}}{\lambda}$, where $\mathbf{r} = (x, y, z)$ are the real-space coordinates and $k = |\mathbf{k}|$. The refocusing of the hologram can be done by eye, similar to the refocusing of a light microscope image as illustrated in Fig. 4, or using autofocus techniques. If the phase shift matches the real-space distance between the reference and the sample, the sample's structure emerges with high contrast and sharp features.

Wiener deconvolution filter. In the last steps, the diffraction patterns were centred based on the reduction of phase ramps in real space and deconvolved using a Wiener deconvolution filter for the cases in which the reference cluster size was well known from radial plots^{38,39}. The reconstruction represents the convolution of the reference and the sample, thus the resolution is often limited by the reference scatterer's size. Using some knowledge about the references, it is possible to resolve even smaller structures with the aid of the Wiener deconvolution filter $F_W(q)$:

$$F_W(q) = \frac{1}{S(q)} \frac{|S(q)|^2 \cdot \text{SNR}(q)}{1 + |S(q)|^2 \cdot \text{SNR}(q)} \quad (4)$$

$S(q)$ describes the estimated diffraction from the reference and $\text{SNR}(q)$ the signal-to-noise ratio. In the current photon energy regime, the diffraction patterns of spherical Xe particles can be well described analytically using Guinier's approximation²⁹ and thus, $S(q)$ can be directly deduced from radial plots.

$\text{SNR}(q)$ is not precisely known but can be estimated using different models. Successful deconvolution with the Wiener filter has been demonstrated on X-ray Fourier holograms in the past based on the model of a constant and adjustable SNR³⁸. The main noise source in our study and in ref. ³⁹ is the shot noise, which scales with the square root of the scattered intensity $I(q)$. Thus, we applied a more realistic model for SNR based on measured data. To check that this more realistic model was appropriate, we tested both approaches on our images. We found that both methods delivered almost identical results.

Resolution estimation. We used the signal-to-noise ratio of the power spectrum of each individual reconstruction to estimate the half-period resolution based on the Rose criterion.

The resolution in Fourier holography is usually limited by several constraints. In the ideal, detector-limited system the resolution is determined by the numerical aperture, whereas in the perfect reference-limited system it is given by the size of the reference scatterer. This limitation is not necessarily imposed by the fact that the reconstruction describes the convolution of both particles. With the knowledge about the reference morphology it becomes possible to deconvolve the reconstruction and therefore resolve even smaller features³⁹. The limitation is thus set by the fact that the signal is modulated by the spectrum of the reference, which has zero crossings. Therefore even the deconvolved reconstruction has a drop in its spectrum that translates into the resolution limit of a perfect reference-limited system. Nevertheless, a deconvolution changes the transmission function within the boundaries of the central speckle of the reference and therefore obtains resolution before the first zero crossing.

In our case, the resolution is limited by photon flux, or in other words, the Poisson noise. Thus, we estimated our resolution from the signal-to-noise ratio in each reconstruction. To estimate the noise level, empty areas at different positions of the Patterson map were used.

The contrast and the resolution of the images can be further improved by changing the number and the material of the references. Several heavy metal nanoparticles such as gold nano-spheres could be used as references. An additional detector placed further downstream could also provide a more complete map of small-angle scattering information and compensate for signal loss due to the FEL passage hole. The upcoming high-repetition-rate X-ray FEL facilities in combination with the newest aerosol injectors will provide thousands of holograms in several minutes and enable 3D imaging of biological specimens with sub-10 nm resolution³¹. The improved approach may enable detailed studies of the internal structure of viruses, such as lipid layers and the nucleic acid.

Hit finding. Bright images were extracted according to the total number of lit pixels and a 2D fast FT (FFT) was calculated. Potential holograms were filtered based on the presence of cross-correlation terms²⁷, which indicate hits where multiple particles were present. Further quality assessment was performed by eye. Within the course of this experiment, the hit rate changed considerably. For example, the Mimi virus hologram displayed in Figs. 2 and 3 was selected from a

run recorded during 15 min at 10 Hz and containing 15 bright holograms of the Mimi virus in total. The holograms from Fig. 5 were extracted from a 10 min run recorded at 30 Hz and containing over 100 holograms. The hologram hit rate varied strongly depending on fine adjustments of both sources. We expect that the hit rate could be significantly improved by recently described injector developments²⁷.

Data availability. The data that support the plots within this paper and other findings of this study are available from the corresponding author upon reasonable request.

References

32. Emma, P. et al. First lasing and operation of an Ångström-wavelength free-electron laser. *Nat. Photon.* **4**, 641–647 (2010).
33. Rupp, D. et al. Identification of twinned gas phase clusters by single-shot scattering with intense soft X-ray pulses. *New. J. Phys.* **14**, 055016 (2012).
34. Rupp, D. et al. Generation and structure of extremely large clusters in pulsed jets. *J. Chem. Phys.* **141**, 044306 (2014).
35. Gutt, C. et al. Single shot spatial and temporal coherence properties of the SLAC LINAC coherent light source in the hard X-ray regime. *Phys. Rev. Lett.* **108**, 024801 (2012).
36. Andritschke, R., Hartner, G., Hartmann, R., Meidinger, N. & Strüder, L. Data analysis for characterizing pnCCDs. In *Nuclear Science Symposium Conference Record 2008* 2166–2172 (IEEE, 2008).
37. Strüder, L. et al. Large-format, high-speed, X-ray pnCCDs combined with electron and ion imaging spectrometers in a multipurpose chamber for experiments at 4th generation light sources. *Nucl. Instrum. Meth. A* **614**, 483–496 (2010).
38. Howells, M. et al. Toward a practical X-ray Fourier holography at high resolution. *Nucl. Instrum. Meth. A* **467**, 864–867 (2001).
39. He, H. et al. Use of extended and prepared reference objects in experimental Fourier transform X-ray holography. *Appl. Phys. Lett.* **85**, 2454–2456 (2004).